$Mn_3MnNb_2O_9$: high-pressure triple perovskite with 1:2 B-site order and modulated spins.

Elena Solana-Madruga,* Clemens Ritter, Cintli Aguilar-Maldonado, Olivier Mentré, J. Paul Attfield and Ángel M. Arévalo-López.*

Supplementary Text:

- **Experimental Methods:**

Ambient pressure $Mn_4Nb_2O_9$ was prepared as described by Bertaut *et al.* [1] and used as a high-pressure precursor in a Pt capsule. 8 GPa and 1100 ˚C were applied using a Walker type module. After temperature quench and slow decompression, the recovered HP_$Mn_4Nb_2O_9$ was characterised using a D2 Bruker diffractometer for sample purity check. Pure samples were studied at room temperature in BL04 Synchrotron beamline at ALBA light source using λ = 0.4128 Å in the 0˚ < 2θ < 40˚ angular range with a 0.003˚ step size. The refined structural parameters are included in Table S1.

High resolution neutron diffraction data were collected at 100 K on the D20 diffractometer at the Institut Laue-Langevin using the 90° takeoff angle and λ = 1.54 Å in the 0˚ < 2θ < 150˚ angular range with a 0.05˚ step size for accurate structural characterisation. Neutron thermodiffraction studies were performed from D20 high intensity data collected at the takeoff angle of 42° on ramping between 5 and 80 K using λ = 2.41 Å and long scans were collected at 5 and 80 K for magnetic structures determination. The magnetic structure below T_M was determined from Rietveld fits against combined NPD data at all measured temperatures between T_N and T_M.

Bulk physical properties were measured using a PPMS 9T Dynacool Quantum Design. Magnetisation was measured in ZFC-FC mode under 1000 Oe, 0.5 T and 1T and a hysteresis loop was collected at 2 K. Heat capacity was measured in the 2-300 K temperature range.

All Rietveld refinements for structural and magnetic characterization were performed using FullProf software package and magnetic symmetry analysis using the BasIreps tool implemented in the FullProf suite of programs. [2] The resulting possible Irreducible representations and their basis vectors are included in Table S2 and the refined parameters in Table S3. The refinement of both magnetic structures involves Irep Γ2, with AFM alignment of the spins along the *c* axis.

- **Magnetic Moment Modulation:**

As described in the main text, the thermal evolution of the magnetic structures can be easily understood by considering the asymmetric magnetic units highlighted into the red square of Fig. 3b. While all MnA sites are AFM coupled, the favoured AFM A-B interactions are not satisfied for Mn2-Mn3 (red) and Mn2-Mn4 (green), thus showing a large magnetic frustration. Representing all Mn sites in octahedral coordination (Fig. S5a) suggests that Mn2-Mn1 (black) AFM interactions through face sharing are stronger than Mn2-Mn3 and Mn2-Mn4, via superexchange through edge sharing. Consistently, B sites align AFM to Mn1 sites in the k_0 phase below T_N.

A comparison of the frustrated interactions between the k_0 phase ($T_M < T < T_N$) and the modulated [⅓ 0 -⅙] phase below T_L is shown in Figure S5, where only half of the low temperature magnetic cell is shown for simplicity along *c*. As discussed, Mn B sites (blue) have two frustrated (FM) interactions with Mn A sites (red and green) in the k_0 phase. This type of units is highlighted in Fig. S6 with a red shadow over the magnetic structure. The pattern of frustrated A-B magnetic interactions into the described asymmetric magnetic units is schematised below the magnetic structure, showing that all units contain two frustrated interactions. The modulation of the magnetic moments into the described sinusoidal and UU0DD0 waves below T_M progressively reduces the number of frustrated interactions down to the ideal pattern shown in the right panel of Fig S.6. As a result of this modulation, two different types of frustrated interactions are found below T_L: the UU0DD0 blue waves retain two FM frustrated interactions every third unit, thus showing a pattern –[0-0-2]–; the sinusoidal waves keep an additional FM interaction with Mn3 with the same periodicity, thus showing a pattern –[1-0-2]–. The units with a single frustrated A-B interaction are highlighted in green over the magnetic structure. The minimum set of units repeated throughout the k_L magnetic phase, containing three asymmetric magnetic units of each type of blue waves, are identified in Fig S.6 with a blue dashed box. The same unit size is used for the k_0 phase in the following calculations for easy comparison.

The relative energy of these two magnetic structures can be estimated using the constraint function $F = -E_f / E_b$, where E_f is the energy associated to the frustrated interactions and E_b is the basis energy of a hypothetical non-frustrated system. [3] The relation between both configurations is therefore $F(k_L)/F(k_0) = E_f(k_L)/E_f(k_0)$. Using a classical spin description, $E_f = \Sigma J_{ij} * s_i * s_j$, where J_{ij} is the spin exchange parameter and s_i and s_j are the magnetic moments of *i* and *j* sites. Here, J_{ij} is identical for all A-B interactions and s values are 2.68 μ_B for all magnetic sites in the k_0 phase as refined from NPD data, 4.33 μ_B for all magnetic

sites in the UU0DD0 waves and 5 and 2.5 μ_B for the maximum and reduced values, respectively, in the sinusoidal waves of the k_L phase. Therefore, all asymmetric magnetic units in the k_0 phase have $E_f = J*s^2 = 7.18*J$, while the units in the UU0DD0 wave at k_L are 29.57*J and those in the sinewave are 23.325*J and 12.5*J (2 and 1 FM interactions respectively). The total E_f in each minimum set of units in the k_L phase is therefore 65.40*J. The $F(k_L)/F(k_0)$ ratio for the same number of units, results in ~ 1.5, revealing that the magnetic moments in the k_0 phase would saturate at 3.3 μ_B. From these calculations, the driving force for the modulation of the magnetic moments is clearly arising from this magnetic frustration, where the development of the SDW allows part of the magnetic moments to saturate the ideal 2S = 5 μ_B for Mn^{2+} cations.

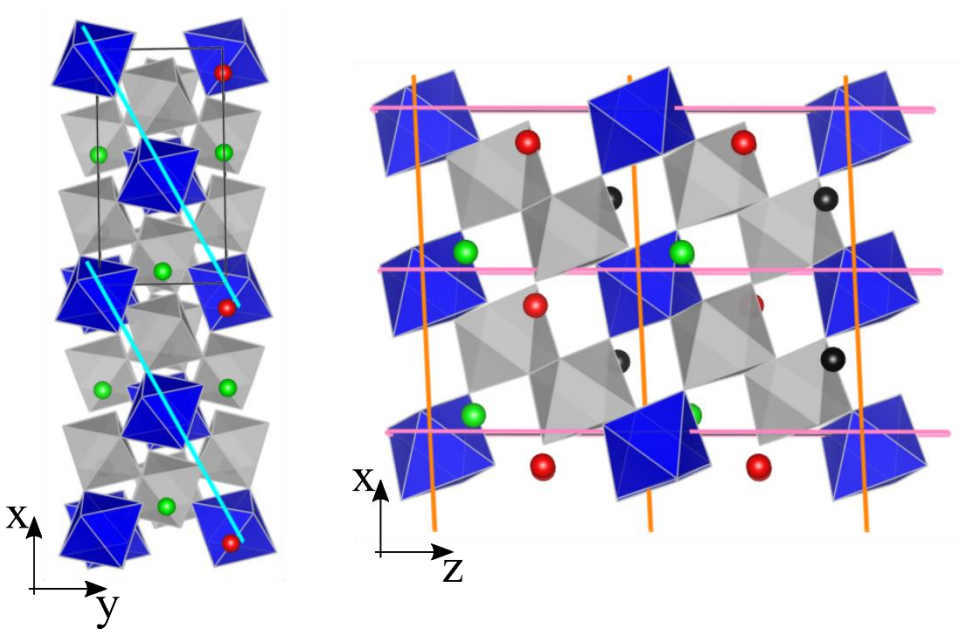

Fig. S1. [001] (left) and [010] (right) projections of the TPv structure of HP- $Mn_3MnNb_2O_9$ showing the cation order into lattice planes (110), (200) and (002) in blue, pink and orange respectively. The stacking of three different layers into each of these planes originates the superstructure peaks observed in SXRD and NPD.

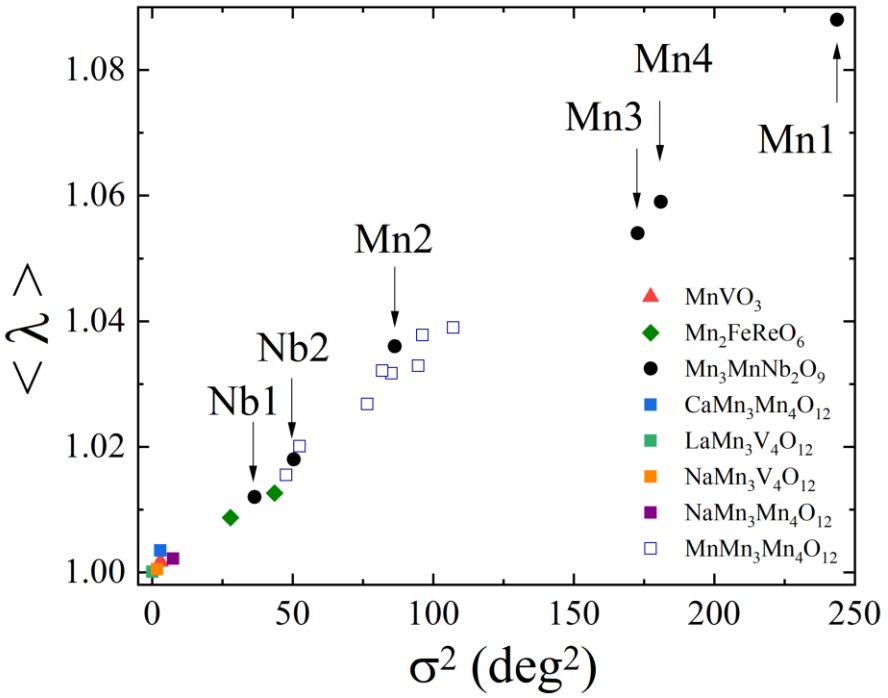

Figure S2. Quadratic elongation / bond angle variance ratio for all cation sites in $Mn_3MnNb_2O_9$ compared to those of the B sites in the reference simple ($MnVO_3$),[4] double (Mn_2FeReO_6),[5] and quadruple ($AMn_3B_4O_{12}$)[6-10] perovskites. The distortion of Nb1, Nb2 and Mn2 sites is comparable to all other values, while that of Mn1, Mn3 and Mn4 is much higher, supporting the TPv structure.

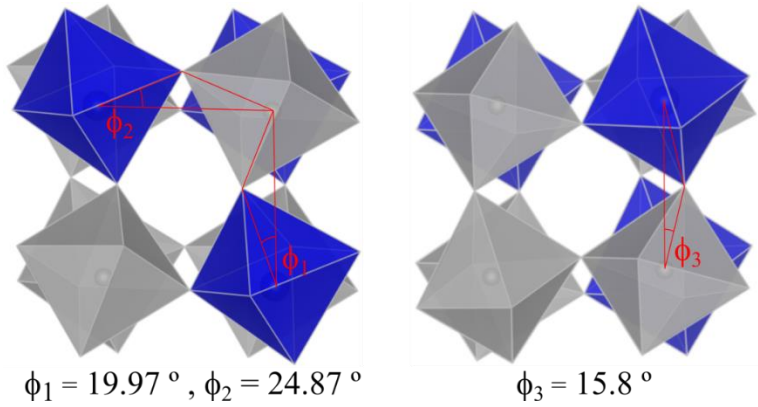

Figure S3. Selected sections of the crystal structure of $Mn_3MnNb_2O_9$ in the same projection as in Fig.1 of the main text (left) and perpendicular to it (right), showing tilt angles Φ_1, Φ_2 and Φ_3 labelled in red.

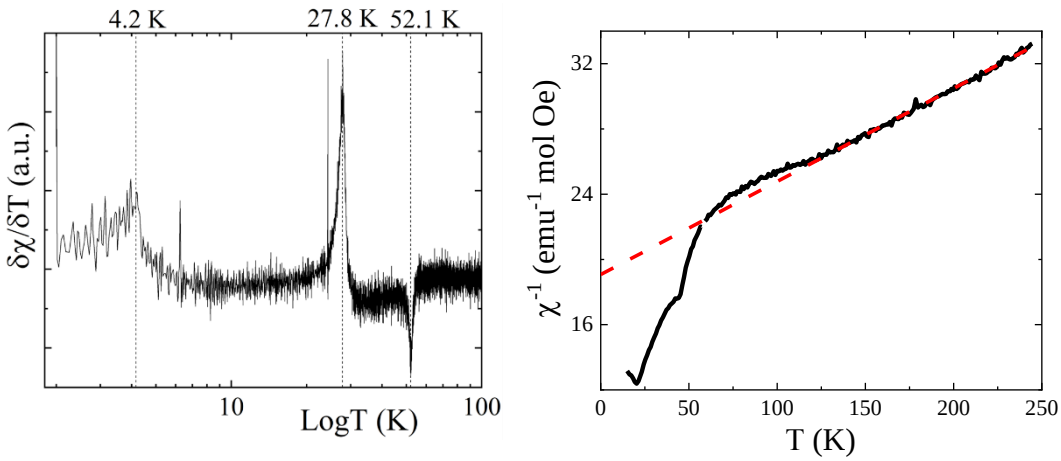

Figure S4. a) ZFC magnetisation derivative curve showing accurate T_N = 52.1 K, T_R = 27.8 K and T_L = 4.2 K values. b) Curie-Weiss fit to the paramagnetic region of the inverse magnetic susceptibility, measured under 1000 Oe. Deviation at 120 K reflects the presence of secondary MnO (19.5(1)% from SXRD). Further optimisation of the HPHT conditions allowed the synthesis of pure HP-$Mn_3MnNb_2O_9$ as shown in the main text.

The magnetic heat capacity of $Mn_3MnNb_2O_9$ has been obtained from neglecting the electronic contribution and removal of the phonon contribution with two Debye terms as:

$$C(T) = A \times 9N_A k_B \left(\frac{T}{T_D}\right) \int_0^{T_D/T} \frac{x^4 e^x}{(e^x-1)^2} dx + B \times 9N_A k_B \left(\frac{T}{T_D}\right) \int_0^{T_D/T} \frac{x^4 e^x}{(e^x-1)^2} dx$$

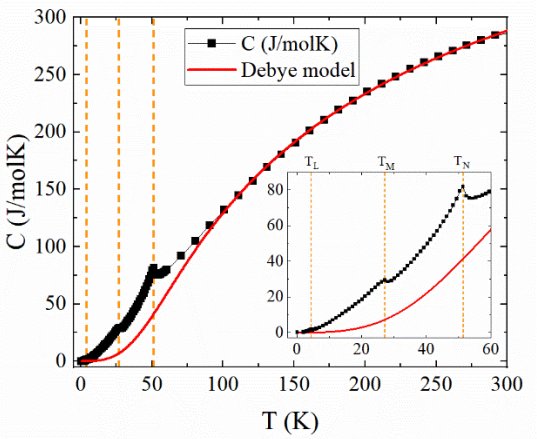

Figure S5. Temperature dependence of $Mn_3MnNb_2O_9$ specific heat (black squares) along with the two terms Deby model used to remove the phonon contribution (red line). The three transitions are marked with vertical orange lines.

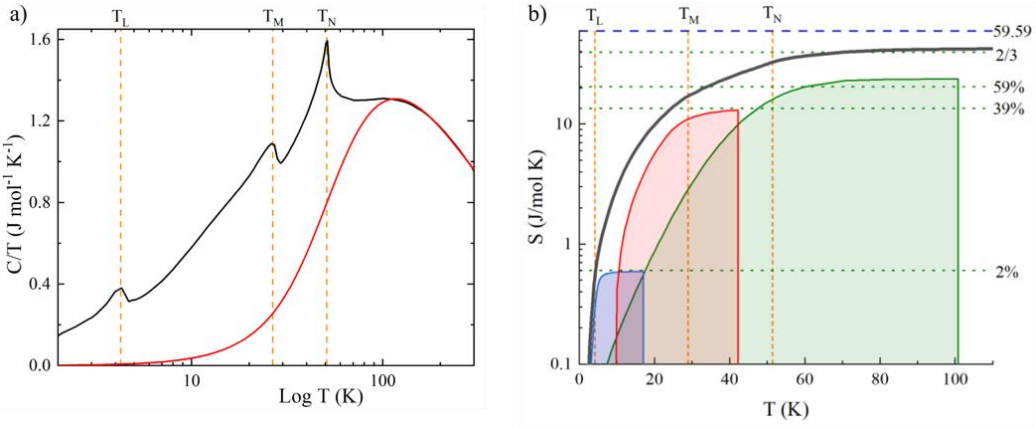

Figure S6. a) C/T and a two Debye model contribution for HP-$Mn_3MnNb_2O_9$. b) Magnetic entropy release of 2/3 respect to the theoretical 59.59 J/molK value. Deconvolution of the entropy contributions at each magnetic transition.

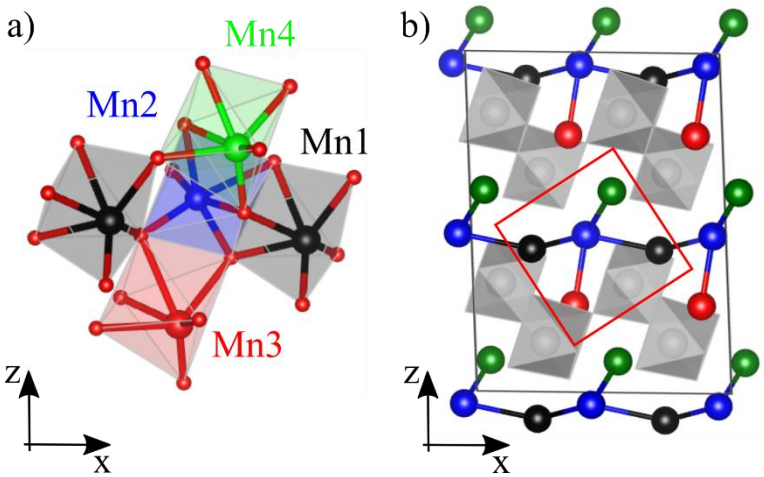

Figure S7. a) Octahedral coordination of Mn sites shown for a magnetic A_4B unit of NN highlighted with a red square in Fig. 3b of the main text and in panel b). Mn2 shares a face with Mn1 to the right, an edge with Mn3 and Mn4 and a corner with Mn1 to the left, all favouring AFM interactions. b) 2D-like magnetic layers with the Mn asymmetric magnetic unit highlighted with a red square.

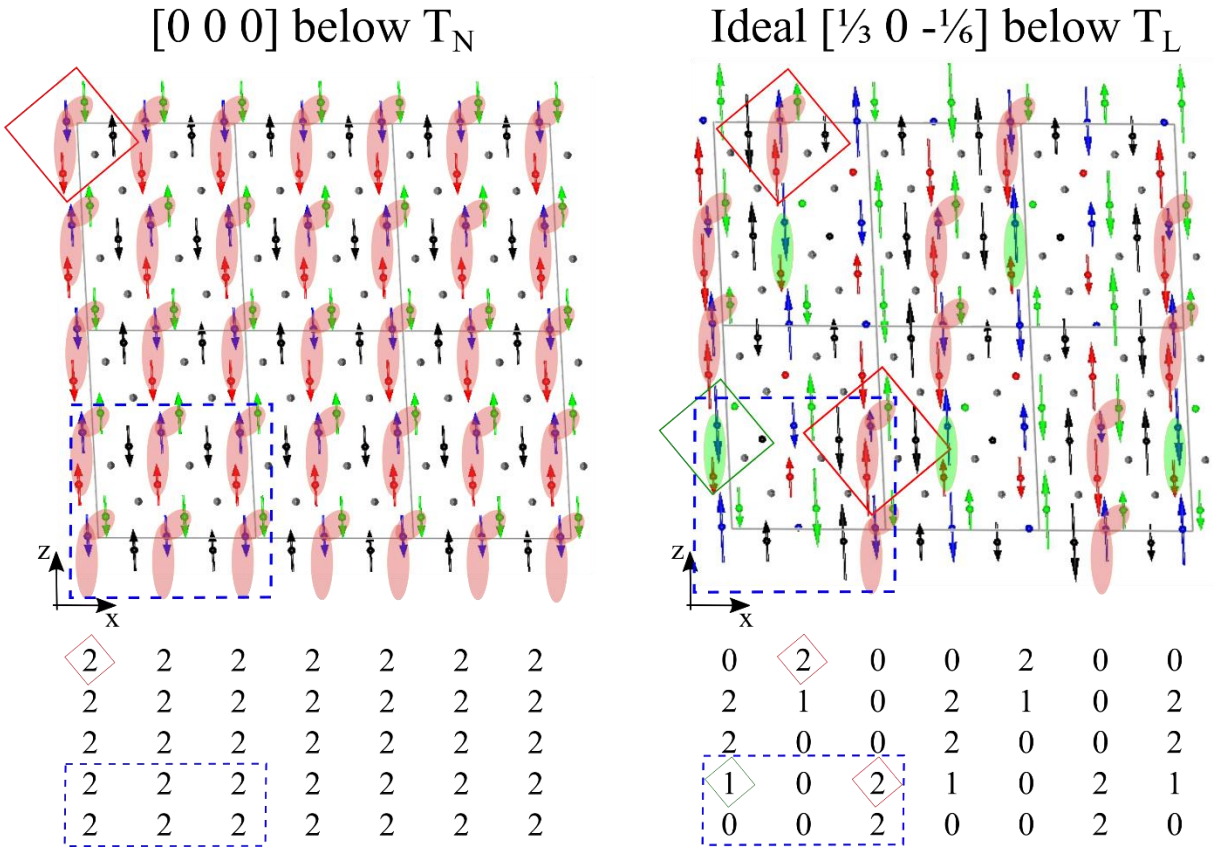

Figure S8. Magnetic structures of the k_0 (left) and k_L (right) phases. Half of the low temperature magnetic cell is shown in both for comparison. Magnetic units identified by the red (or green) squares are shown to have 2 (red shadow), 1 (green shadow) or none (no shadow) frustrated magnetic interactions. Below each panel, the schematic patterns of magnetic frustrated interactions are shown for the same cell size. Blue dashed rectangle identifies the smallest set of asymmetric magnetic units rolling throughout the k_L phase and thus determining the constraint function as detailed in supplementary text.

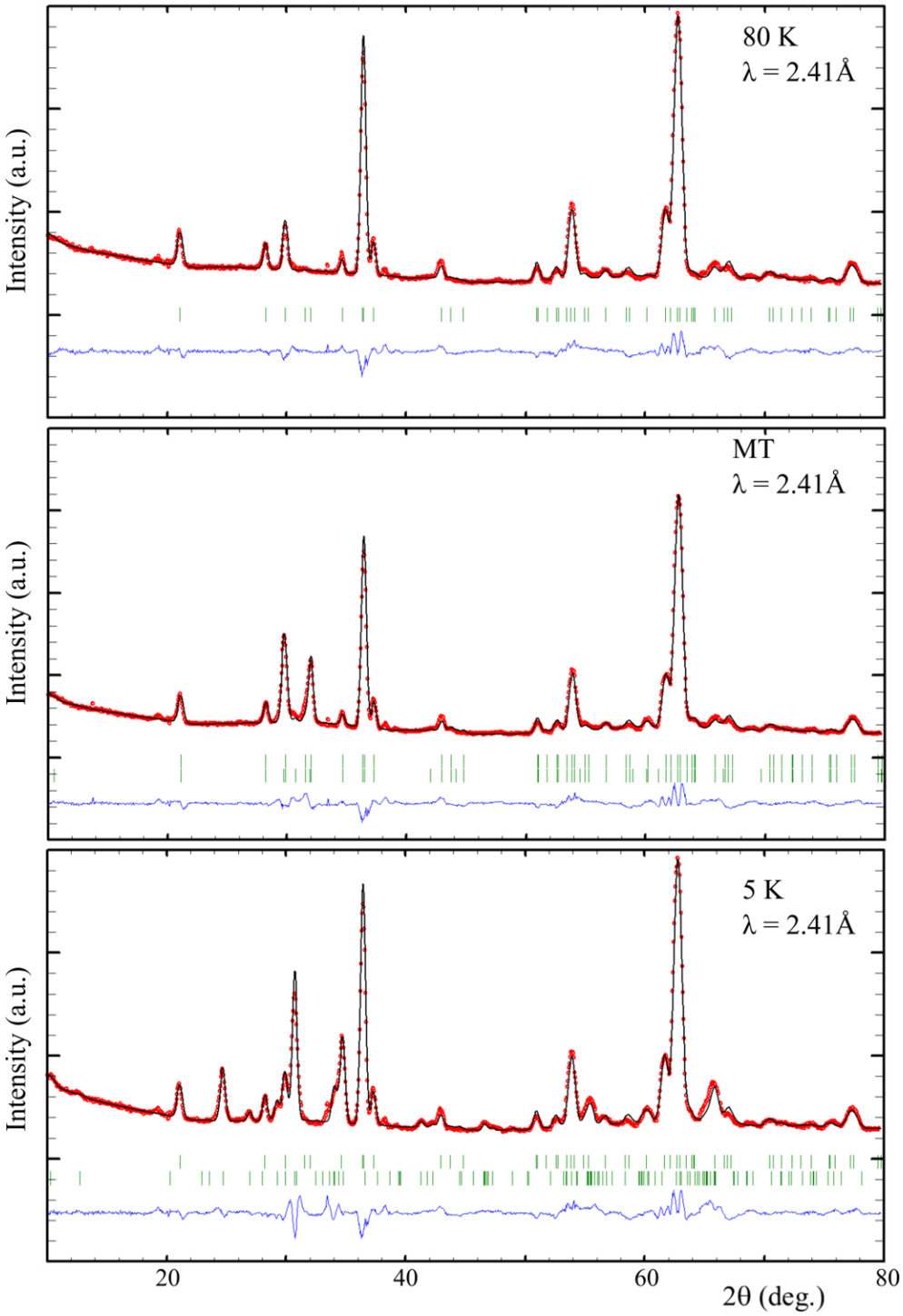

Figure S9. Rietveld fits of the NPD data collected at 80, MT (for medium temperature, sum of all data collected at $T_M < T < T_N$) and 5 K using λ = 2.41 Å.

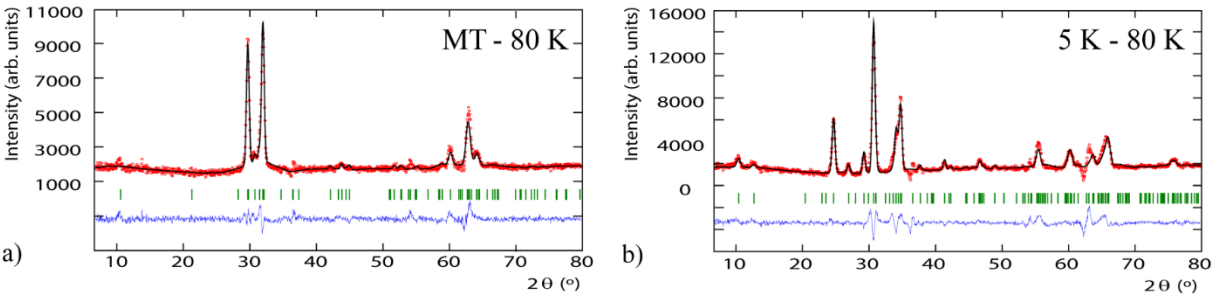

Figure S10. Rietveld fits of the NPD MT – 80 K and 5 K – 80 K difference patterns using the collinear (a) and SDW (b) magnetic models respectively.

Table S1**.** Main crystallographic features refined from 300 K SXRD data. S.G. *Cc* and cell parameters *a* = 9.9191(2) Å, *b* = 5.3358(1) Å, *c* = 13.2276(4) Å and *β* = 92.725(2) °. Agreement factors: R_p = 12.9%, R_{wp} = 16.8 %, R_B = 5.19%, R_f = 3.96%, χ^2 = 3.09%.

Site	*x*	*y*	*z*	Biso (Å^2)	Occ
Mn1	0.727(1)	0.500(4)	0.428(1)	0.43(2)	1.0
Mn2	0.440(3)	0.505(5)	0.499(2)	0.43(2)	1.0
Mn3*	0.394	0.5	0.757	0.43(2)	1.0
Mn4	0.559(1)	0.014(4)	0.591(1)	0.43(2)	1.0
Nb1	0.106(1)	0.508(3)	0.837(1)	0.43(2)	1.0
Nb2	0.771(1)	0.509(2)	0.665(1)	0.43(2)	1.0
O1	0.733(7)	0.698(2)	0.795(6)	0.43(2)	1.0
O2	0.192(6)	0.670(2)	0.712(6)	0.43(2)	1.0
O3	0.121(6)	0.887(5)	0.076(4)	0.43(2)	1.0
O4	0.852(6)	0.349(2)	0.547(5)	0.43(2)	1.0
O5	0.515(6)	0.648(2)	0.381(5)	0.43(2)	1.0
O6	0.572(7)	0.188(2)	0.461(7)	0.43(2)	1.0
O7	0.802(6)	0.895(5)	0.415(4)	0.43(2)	1.0
O8	0.467(7)	0.894(6)	0.748(6)	0.43(2)	1.0
O9	0.401(9)	0.306(1)	0.617(6)	0.43(2)	1.0

* Mn3 site used as a cell reference.

Table S2. Irreducible representations (Irep) and basis vectors (BV) for HP-$Mn_3MnNb_2O_9$ using BasIreps under k_0 = [0 0 0] (top) and k_L = [k_x 0 k_z] (bottom). Upper and lower sets of values for each BV are real and imaginary components respectively.

k_0 = [0 0 0]	**Γ_1**			**Γ_2**		
	BV1	BV2	BV3	BV1	BV2	BV3
x y z	1 0 0	0 1 0	0 0 1	1 0 0	0 1 0	0 0 1
	0 0 0	0 0 0	0 0 0	0 0 0	0 0 0	0 0 0
x -y z+1/2	1 0 0	0 -1 0	0 0 1	-1 0 0	0 1 0	0 0 -1
	0 0 0	0 0 0	0 0 1	0 0 0	0 0 0	0 0 0
k_L = [k_x 0 k_z]	**Γ_1**			**Γ_2**		
	BV1	BV2	BV3	BV1	BV2	BV3
x y z	2.0757 0 0	0 2.0757 0	0 0 2.0757	2.0757 0 0	0 2.0757 0	0 0 2.0757
	0 0 0	0 0 0	0 0 0	0 0 0	0 0 0	0 0 0
x -y z+1/2	1.819 0 0	0 -1.819 0	0 0 1.819	-1.819 0 0	0 1.819 0	0 0 -1.819
	1 0 0	0 -1 0	0 0 1	-1 0 0	0 1 0	0 0 -1

Table S3. Refined magnetic moments using BV3 of Γ_2 for both magnetic structures. Propagation vector and magnetic phases between different Mn sites are also included for the $k_L = [k_x\ 0\ k_z]$ structure.

	$k_0 = [0\ 0\ 0]$	$k_L = [k_x\ 0\ k_z]$
μ (μ_B)	2.68(1)	5.1(1)
mphase Mn1	0	-0.383(6)
mphase Mn2	0	-0.121(4)
mphase Mn3	0	0
mphase Mn4	0	-0.380 (6)
k_x	0	0.3361(2)
k_z	0	0.8516(6)

References

[1] E. F. Bertaut, L. Corliss, F. Forrat. *J. Phys. Chem. Solids.* **1961**, *21*, 234.

[2] J. Rodriguez-Carvajal, *Physica B*, **1993**, *192*, 55.

[3] D. Dai, M.H. Whangbo, J. Chemical Physics, **2004**, *121*, 672.

[4] M. Markkula, A. M. Arevalo-Lopez, A. Kusmartseva, J. A. Rodgers, C. Ritter, H. Wu, J. P. Attfield. Phys. Rev. B, 2011, 84, 094450.

[5] a) A.M. Arévalo-López, G.M. McNally, J.P. Attfield, Angew. Chem. Int. Ed. 2015, 54, 12074-12077. b) M.R. Li, M. Retuerto, Z. Deng, P.W. Stephens, M. Croft, Q. Huang, H. Wu, X. Deng, G. Kotliar, J. Sánchez-Benítez, J. Hadermann, D. Walker, M. Greenblatt, Angew. Chem. Int. Ed. 2015, 54, 12069-12073.

[6] A. A. Belik, Y. S. Glazkova, Y. Katsuya, M. Tanaka, A. V. Sobolev, I. A. Presniakov, *J. Phys. Chem. C* **2016**, *120*, 8278−8288

[7] Y. Shimakawa, S. Zhang, T. Saito, M. W. Lufaso, P. M. Woodward, *Inorg. Chem.* **2014**, *53*, 594−599.

[8] S. Zhang, T. Saito, M. Mizumaki, W.-T Chen, T. Tohyama, Y. Shimakawa, *J. Am. Chem. Soc.* **2013**, *135*, 6056−6060.

[9] M. Marezio, P. D.Dernier, J. Chenavas, J. C. Joubert, *J. Solid State Chem.* **1973**, *6*, 16-20.

[10] S. V. Ovsyannikov, A. M. Abakumov, A. A. Tsirlin, W. Schnelle, R. Egoavil, J. Verbeeck, G. Van Tendeloo, K. V. Glazyrin, M. Hanfland, L. Dubrovinsky. *Angew. Chem. Int. Ed.* **2013**, *52*, 1494-1498.

Author Contributions

The study was designed by AMAL. Synthesis was performed by ESM and CAM. Bulk magnetism and heat capacity data were measured and analysed by ESM, CAM and AMAL. Syncrhtotron data were collected and analysed by ESM and AMAL. Neutron diffraction data were collected and analysed by ESM, AMAL and CR. The paper was written by ESM and AMAL with collaborations from all authors.